Enhanced photocatalytic performance of CuBi$_2$O$_4$ particles decorated with Ag nanowires

CrossMark

Fei Wang[a,b], Hua Yang[a,b,*], Yunchuan Zhang[b]

[a] State Key Laboratory of Advanced Processing and Recycling of Non-ferrous Metals, Lanzhou University of Technology, Lanzhou 730050, China
[b] School of Science, Lanzhou University of Technology, Lanzhou 730050, China

A R T I C L E   I N F O

Keywords:
CuBi$_2$O$_4$ particles
Ag nanowires
Ag-CuBi$_2$O$_4$ composite
Enhanced photocatalytic activity
Photocatalytic mechanism

A B S T R A C T

CuBi$_2$O$_4$ particles (350–700 nm) were decorated with Ag nanowires (30 nm in diameter and 0.8–1.5 μm in length) by a hydrothermal route. The as-prepared Ag-CuBi$_2$O$_4$ composite was systematically characterized by XRD, TEM, XPS, UV–vis DRS, EIS, PL spectroscopy and photocurrent response. It is revealed that Ag-CuBi$_2$O$_4$ composite displays an enhanced separation efficiency of photogenerated electron-hole pairs, which is due to the migration of electrons from CuBi$_2$O$_4$ particles to Ag nanowires. RhB and phenol were chosen as the target organic pollutant to evaluate their degradation behavior over the samples under simulated-sunlight irradiation. It is observed that Ag-CuBi$_2$O$_4$ composite shows a photocatalytic activity much higher than that of bare CuBi$_2$O$_4$. The enhanced photocatalytic activity of the composite can be explained by the efficient separation of photo-induced charges and the increased availability of the charges for the photocatalytic reactions. The reactive species were determined by investigating the effect of ethanol, BQ and AO on the degradation of RhB and the formation of •OH radicals. It is concluded from the experimental results that •OH is the dominant reactive species causing the dye degradation. The photocatalytic mechanism involved was discussed.

1. Introduction

Spinel-type compounds with general formula of AB$_2$O$_4$ (where A represents a divalent metal cation and B represents a trivalent metal cation) have attracted extensive interest due to their diverse properties and wide applications in electronic devices, catalysis and energy storage. Copper bismuth oxide (CuBi$_2$O$_4$), packed with square planar CuO$_4$ groups linked to distorted trigonal BiO$_6$ polyhedra [1], is one of the outstanding representatives of spinel-type compounds. CuBi$_2$O$_4$ is a p-type semiconductor and holds many promising physicochemical properties including magneticity, dielectricity, high-temperature heat capacity, electrochemical capacitance, photoelectrochemical property and catalysis [2–24]. In particular, CuBi$_2$O$_4$ has a relatively small bandgap energy of 1.5–1.9 eV, and thus it can largely absorb the visible part of the solar spectrum. As the photocatalytic applications, Bi-contained semiconductors are particularly interesting [25–27], and furthermore, the conduction band potential of CuBi$_2$O$_4$ is more negative than the redox potential of H$^+$/H$_2$. Due to these attractive features, CuBi$_2$O$_4$ has been extensively studied as a photocathode for solar water splitting into H$_2$ [11–15]. It has been shown that CuBi$_2$O$_4$ can be also used as a promising visible-light-responsive photocatalyst for the degradation of organic dye pollutants [19–24].

The photocatalytic behavior of a semiconductor is closely associated with photogenerated electrons (e$^-$) and holes (h$^+$). For a bare semiconductor, however, most of the photogenerated electrons and holes will undergo rapid geminate recombination and only a small portion of the carriers migrate to the semiconductor surface for participating in the photocatalytic reactions. Efficient separation of electron-hole pairs is crucial to achieve a good photocatalytic activity of the semiconductor. Construction of heterostructured composites from two semiconductors is one of the most important strategies to promote the electron-hole pair separation and hence improve the photocatalytic performance of semiconductors. Recently, much work has been devoted to the heterostructure composite photocatalysts constructed from CuBi$_2$O$_4$ and other semiconductors, such as CuBi$_2$O$_4$/TiO$_2$, CuBi$_2$O$_4$/BiVO$_4$, CuBi$_2$O$_4$/SrO, CuBi$_2$O$_4$/CeO$_2$, CuBi$_2$O$_4$/NaTaO$_3$ and CuBi$_2$O$_4$/Bi$_2$WO$_6$ [28–34]. In these composites, photogenerated electrons or holes tend to migrate from one semiconductor to another. Due to this carrier transfer process, the recombination rate of electron-hole pairs can be effectively inhibited, and thus more carriers are available for the photocatalytic reactions. It has been shown that these composite photocatalysts exhibit significantly enhanced photocatalytic activity compared to individual semiconductors. Decoration of the semiconductor with noble metals (e.g. Ag, Au, Pt, etc.) is another promising strategy to

---

improve its photocatalytic activity [35–37]. Noble metals that act as efficient electron sinks can capture photogenerated electrons, leaving behind holes on the semiconductor surface. As a result, photogenerated holes are increasingly available to participate in the photocatalytic reactions. Up to now, there has been little work concerned with the photocatalytic performance of noble metal-decorated $CuBi_2O_4$ photocatalyst. In this work, we adopted a hydrothermal route to grow Ag nanowires onto the surface of $CuBi_2O_4$ particles. The photocatalytic performance and mechanism of the as-prepared Ag-$CuBi_2O_4$ composites was investigated by degrading rhodamine B (RhB) and phenol under simulated-sunlight irradiation.

2. Experimental

2.1. Preparation of CuBi₂O₄ particles

$CuBi_2O_4$ particles were synthesized via a polyacrylamide gel route as described in the literature [38]. In a typical synthesis process, 4.8507 g (0.01 mol) of $Bi(NO_3)_3 \cdot 5H_2O$ and 1.208 g (0.005 mol) of $Cu(NO_3)_2 \cdot 3H_2O$ were dissolved in 30 mL of dilute nitric acid solution. Then 3.377 g (0.0225 mol) of tartaric acid, 20 g of glucose, and 9.5958 g (0.135 mol) of acrylamide were successively added to the above solution. The molar amount of tartaric acid and acrylamide was 1.5 and 9 times the amount of total Cu^{2+}/Bi^{3+} ions, respectively. During the process of adding chemical reagents, the solution was subjected to stirring using a magnetic stirrer to ensure the additives dissolved completely. The mixture solution was made up to 100 mL by adding distilled water, and then heated up to 80 °C and maintained at this temperature on a hot plate for 3 h. The formed gel was dried at 120 °C for 12 h in a thermostatic drier. The obtained xerogel was ground into powder in a mortar and placed inside a tubular furnace for calcination at 600 °C. After 10 h of calcination, the tubular furnace was cooled down to room temperature naturally, finally yielding $CuBi_2O_4$ particles.

2.2. Decoration of CuBi₂O₄ particles with Ag nanowires

1 g of as-prepared $CuBi_2O_4$ particles was loaded in 30 mL of ethylene glycol and subjected to ultrasonic treatment for 30 min to make the particles disperse uniformly. 0.1 g of polyvinyl pyrrolidone (PVP), 0.1 g of $AgNO_3$ and 2 mg of NaCl were dissolved in 20, 20 and 10 mL of ethylene glycol, respectively. The three solutions were successively added to the above $CuBi_2O_4$ suspension slowly (drop by drop). The obtained mixture was transferred to and sealed in a Teflon-lined stainless-steel autoclave of 100 mL capacity and submitted to hydrothermal treatment at 160 °C. After 5 h of reaction, the autoclave was naturally cooled down to room temperature. During the hydrothermal process, Ag nanowires were grown onto $CuBi_2O_4$ particles. The product was collected and washed several times with acetone and absolute ethanol, and then dried in a thermostated drying oven at 60 °C for 2 h to obtain the final Ag-$CuBi_2O_4$ composite.

2.3. Sample characterization

The structural analysis of the samples was carried out using x-ray powder diffraction (XRD) with Cu Kα radiation (λ = 0.15406 nm). The morphology and microstructure of the samples was observed by field-emission scanning electron microscopy (SEM) and field-emission transmission electron microscopy (TEM). The N_2 adsorption/desorption technique was used to measure the Brunauer–Emmett–Teller (BET) specific surface area of the samples. The electron binding energies for the elements were measured by x-ray photoelectron spectroscopy (XPS), where the binding energy scale of the XPS data was calibrated against the adventitious C 1 s peak at the binding energy of 284.8 eV. The optical absorption and bandgap energy of the samples was investigated by ultraviolet-visible diffuse reflectance spectroscopy

(UV–vis DRS) on a UV–vis spectrophotometer with an integrating sphere attachment. The photoluminescence (PL) spectrum of the samples was measured on a fluorescence spectrophotometer with the excitation wavelength of 320 nm.

2.4. Photoelectrochemical measurement

The electrochemical impedance spectroscopy (EIS) and photocurrent response measurements were performed on a CST 350 electrochemical workstation using a three-electrode cell configuration, which consists of working electrode, a platinum foil as the counter electrode and a standard calomel electrode (SCE) as the reference electrode. 0.1 mol L^{-1} Na_2SO_4 aqueous solution was used as the electrolyte. A 200 W Xenon lamp was used as the light source. The working electrode was prepared as follows. 15 mg of $CuBi_2O_4$ or Ag-$CuBi_2O_4$, 0.75 mg of carbon black and 0.75 mg of polyvinylidene fluoride (PVDF) were mixed together using 1-methyl-2-pyrrolidone (NMP) as solvent to form slurry. The slurry was uniformly coated onto fluorine-doped tin oxide (FTO) glass substrate with area of 1 × 1 cm^2, and then submitted to drying at 60 °C for 5 h in a thermostat drying oven. The EIS spectra were recorded by applying an alternating current (AC) voltage with amplitude of 5 mV and in the frequency range of 10^{-2} to 10^5 Hz. The transient photocurrents were measured at a fixed bias potential of 0.2 V.

2.5. Photocatalytic test

RhB and phenol were used as the target organic pollutant to evaluate the photocatalytic activity of the samples under simulated-sunlight irradiation. The photoreactor configuration is schematically shown in Fig. 1. The initial concentration of RhB or phenol was 2 mg L^{-1}. As a typical photocatalytic process, 0.1 g of $CuBi_2O_4$ or Ag-$CuBi_2O_4$ was loaded in 100 mL of RhB or phenol solution, to which was then added 1 mL of H_2O_2. The mixture was magnetically stirred for 30 min in the dark in order to attain the adsorption/desorption equilibrium of RhB onto the photocatalyst surface. After that, the mixture was irradiated by a 200 W xenon lamp. During the photocatalysis process, the reaction solution was kept at room temperature by cooling the photocatalytic reactor with a water-cooling system. At intervals of 10 min, 3 mL of the reaction solution was taken out from the reactor and centrifuged at 4000 r min^{-1} for 10 min to remove the photocatalyst. The absorbance of the upper clear solution in the centrifuge tube was measured at 554 nm for RhB or 270 nm for phenol using a UV–vis spectrophotometer. According to the absorbance, the RhB or phenol concentration of the reaction solution was then determined. In order to reveal the reactive species in the Ag-$CuBi_2O_4$ photocatalytic system, we investigated the effect of ethanol, benzoquinone (BQ) and ammonium oxalate (AO) on the degradation of RhB. Here ethanol, BQ and AO are used as the scavengers of hydroxyl (•OH), superoxide (•O_2^-) and h^+, respectively. 5 mL of ethanol, 0.0011 g of BQ and 0.0142 g of AO are separately added in 100 mL reaction solution, and then the

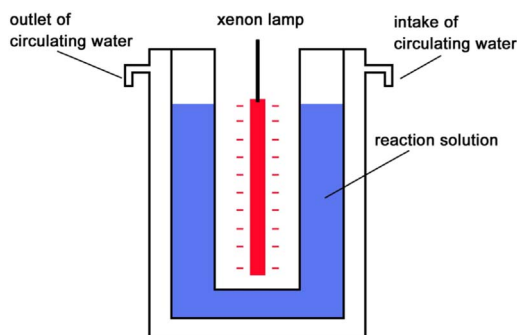**Fig. 1.** Schematic illustration of the photoreactor configuration.

photocatalytic experiments are carried out under the same conditions.

2.6. Detection of hydroxyl

•OH radicals generated in the photocatalytic system were examined by PL spectroscopy using terephthalic acid (TPA) as a •OH scavenger. It is established that TPA can react with •OH to produce 2-hydroxyterephthalic acid (TAOH), which can emit photoluminescence having wavelength of 429 nm [39]. A stoichiometric amount of TPA was dissolved in NaOH aqueous solution ($1.0 \, mmol \cdot L^{-1}$) to make a $0.25 \, mmol \, L^{-1}$ TPA solution. 0.1 g of the photocatalyst and 1 mL of H_2O_2 were added in 100 mL of the TPA solution, followed by magnetic stirring for 30 min in the dark. The mixture was then irradiated by a 200 W xenon lamp. After reaction for 30 min, a small portion of the solution was pipetted out and centrifuged at $4000 \, r \, min^{-1}$ for 10 min to remove the photocatalyst. The PL spectrum of the upper clear solution in the centrifuge tube was measured at a fluorescence spectrophotometer with an excitation wavelength of 315 nm. To investigate the effect of ethanol, BQ and AO on the formation of •OH radicals, 5 mL of ethanol, 0.0011 g of BQ and 0.0142 g of AO are separately added in 100 mL TPA reaction solution, and then the PL measurement follows the same process as described above.

3. Results and discussion

Fig. 2 shows the XRD patterns of $CuBi_2O_4$ and $Ag\text{-}CuBi_2O_4$ samples, along with the standard XRD line patterns for $CuBi_2O_4$ tetragonal structure with $P4/ncc$ space group (PDF #42-0334) and Ag cubic structure with $Fm\text{-}3m$ space group (PDF #04-0783). It is seen that all the diffraction peaks for $CuBi_2O_4$ can be indexed according to the standard diffraction pattern, implying that the particles crystallize into single $CuBi_2O_4$ tetragonal phase. For $Ag\text{-}CuBi_2O_4$, the XRD pattern shows that $CuBi_2O_4$ undergoes no structural change and maintain the tetragonal structure. However, additional weak diffraction peaks from Ag cubic phase are visible in the XRD pattern, indicating the formation of Ag nanowires in the composite.

Fig. 3(a) shows the SEM image of $CuBi_2O_4$ particles, revealing that the particles are shaped like spheres or polyhedrons. The primary particle size distribution (measured by Heywood diameter) ranges from 350 to 700 nm and the average size of the particles is estimated to be 550 nm. Fig. 3(b) shows the SEM image of $Ag\text{-}CuBi_2O_4$ composite, from which one can see that Ag nanowires are decorated onto $CuBi_2O_4$ particles. These Ag nanowires have the same diameter of 30 nm but different lengths ranging from 0.8 to 1.5 μm. The BET specific surface

area of $CuBi_2O_4$ and $Ag\text{-}CuBi_2O_4$ is measured by the N_2 adsorption/desorption technique as 12.4 and $14.9 \, m^2 \, g^{-1}$, respectively. The introduction of Ag nanowires leads to a slight increase in the BET specific surface area of the resultant $Ag\text{-}CuBi_2O_4$ composite. This can be attributed to the fact that Ag nanowires have relatively higher BET specific surface area than $CuBi_2O_4$ particles.

The microstructure of $Ag\text{-}CuBi_2O_4$ composite was investigated by TEM. Fig. 4(a) shows the TEM image of $Ag\text{-}CuBi_2O_4$, revealing that $CuBi_2O_4$ particles with size of 400–600 nm are decorated with Ag nanowirs of 30 nm in diameter and 0.8–1.5 μm in length. The morphology and size of $CuBi_2O_4$ particles and Ag nanowirs observed by TEM basically agrees with that observed from the SEM image. Fig. 4(b) shows the high resolution TEM (HRTEM) image of $Ag\text{-}CuBi_2O_4$. It is clear that both $CuBi_2O_4$ particles and Ag nanowires display perfect crystal lattice fringes, implying that they have a good crystallization. The crystal lattice fringes of $CuBi_2O_4$ with an interplanar distance of 0.425 nm correspond to the (200) crystal plane of $CuBi_2O_4$, and the crystal lattice fringes of Ag have an interplanar distance of 0.236 nm and are assignable to the Ag (111) crystal plane. Fig. 4(c) shows the dark-field scanning TEM (DF-STEM) image of $Ag\text{-}CuBi_2O_4$, and Fig. 4(d)–(g) give the corresponding elemental mapping images of the region indicated in Fig. 4(c). It is seen that the large-sized particles present the elemental distribution of Cu, Bi and O, and are therefore confirmed to be $CuBi_2O_4$ particles. No obvious chemical composition segregation is observed in the $CuBi_2O_4$ phase. The nanowires assembled onto $CuBi_2O_4$ particles display the elemental distribution of Ag, confirming that they are Ag nanowires. The chemical composition of $Ag\text{-}CuBi_2O_4$ is further investigated by the energy-dispersive x-ray spectroscopy (EDS). Fig. 4(h) shows the EDS spectrum of $Ag\text{-}CuBi_2O_4$. It is noted that EDS is sensitive to heavy elements like Cu, Bi and Ag, but not to light elements like O. As a result, the EDS spectrum presents obvious signals of Cu, Bi and Ag elements, but a weak signal of O element. The atomic ratio of Cu to Bi is obtained as 1.75/1, which is much higher than the Cu/Bi atomic ratio (1/2) of $CuBi_2O_4$ phase. The observation of high-intensity Cu signal could be ascribed to the contribution of the Cu microgrid used for supporting the sample. The atomic ratio of Ag to Bi is obtained as 0.277/1, implying about 5.2 wt% of Ag nanowires in the composite.

The elemental oxidation state of $CuBi_2O_4$ and $Ag\text{-}CuBi_2O_4$ was investigated by XPS. Fig. 5(a) shows the XPS survey scan spectra of the samples, revealing the presence of the elements Cu, Bi and O in both the samples. Moreover, additional Ag signal is clearly included in the XPS spectrum of the composite. The observed C signal at 284.8 eV arises from adventitious carbon used for calibration of the binding energy scale. Fig. 5(b)–(d) show the XPS spectra of Cu 2p, Bi 4f and O 1s, respectively. The XPS signals for $CuBi_2O_4$ are seen to be very similar to those for $Ag\text{-}CuBi_2O_4$, suggesting that the decoration of Ag nanowires onto $CuBi_2O_4$ particles cannot lead to an obvious change in the elemental oxidation state. On the Cu 2p XPS spectra shown in Fig. 5(b), the peaks at 934.1 and 953.8 eV are attributed to the binding energies for Cu $2p_{3/2}$ and Cu $2p_{1/2}$, respectively, and the peaks at 942.3 and 962.6 eV are characterized to be the satellite peaks of Cu 2p. The Cu 2p peak positions and the presence of satellite peaks confirm that the copper species exists in the $+2$ oxidation state. The Bi 4f XPS spectra given in Fig. 5(c) show two sharp peaks at 158.6 and 163.9 eV, which are assigned to the binding energies of Bi $4f_{7/2}$ and Bi $4f_{5/2}$, respectively. This is indicative of the presence of Bi^{3+} oxidation state. The O 1s XPS signals shown in Fig. 5(d) are deconvoluted into three peaks separately at 529.8, 531.6 and 532.9 eV. The main peak at 529.8 eV arises from the contribution of the crystal lattice oxygen. The peaks at higher binding energies could arise due to surface defects or chemisorbed oxygen species [40]. Fig. 5(e) shows the Ag 3d XPS spectrum, where the peaks at 367.9 and 373.9 eV are assigned to the binding energies for Ag $3d_{5/2}$ and Ag $3d_{3/2}$, respectively, implying the existence of Ag^0 metalstate. The presence of Ag^+ oxidationstate in the composite can be excluded because no additional peaks are visible on the spectrum.
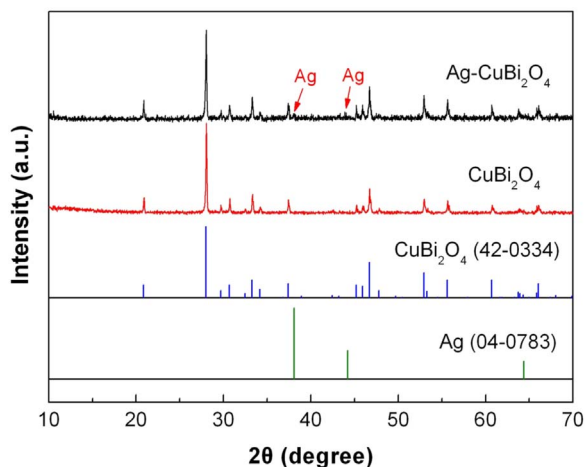

Fig. 2. XRD patterns of $CuBi_2O_4$ and $Ag\text{-}CuBi_2O_4$, along with the standard XRD line patterns for $CuBi_2O_4$ tetragonal structure (PDF #42-0334) and Ag cubic structure (PDF #04-0783).

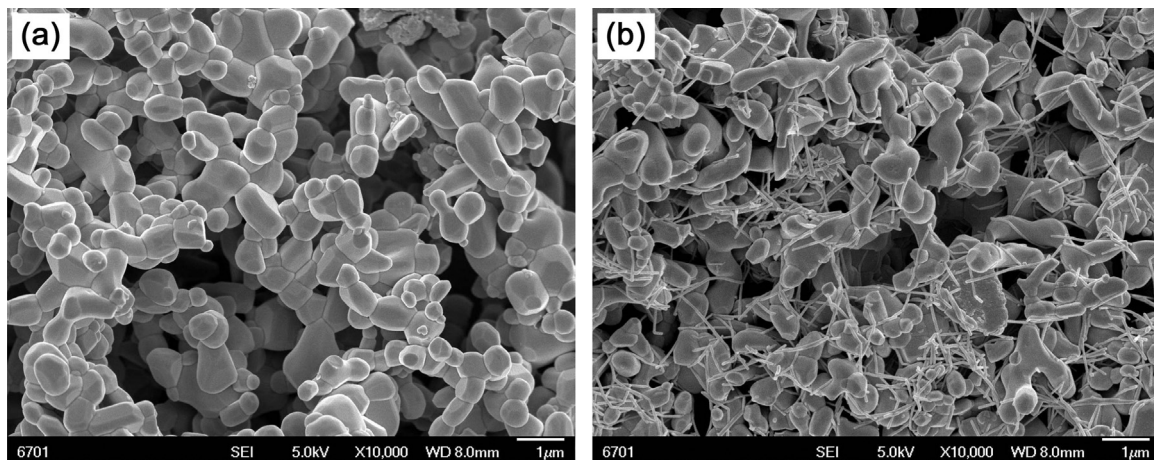**Fig. 3.** SEM images of (a) CuBi₂O₄ and (b) Ag-CuBi₂O₄.

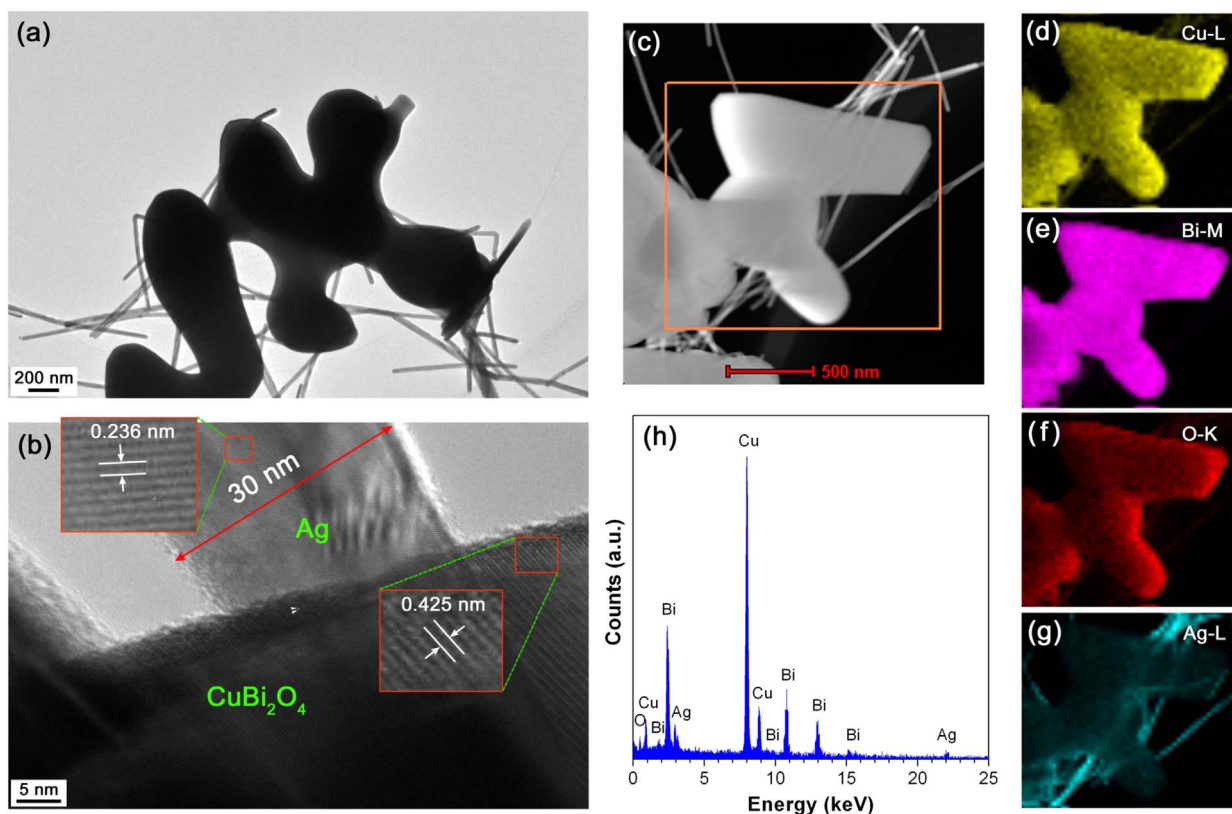**Fig. 4.** (a) TEM image of Ag-CuBi₂O₄. (b) HRTEM image of Ag-CuBi₂O₄. (c) DF-STEM image of Ag-CuBi₂O₄. (d)–(g) The corresponding elemental mapping images of the region indicated in (c). (h) EDX spectrum of Ag-CuBi₂O₄.

Fig. 6(a) shows the UV–vis DRS spectra of CuBi₂O₄ and Ag-CuBi₂O₄, and the corresponding first derivative spectra are shown in Fig. 6(b). Compared to bare CuBi₂O₄, Ag-CuBi₂O₄ composite has enhanced absorption in the visible light region, which will improve the utilization rate of photons. The absorption edge of the samples can be obtained from the peak on the first derivative spectra. For bare CuBi₂O₄, the absorption edge is observed at 654.7 nm, from which its bandgap energy is obtained as 1.89 eV. For Ag-CuBi₂O₄ composite, the absorption edge undergoes no shift, implying a negligible change in the bandgap energy of CuBi₂O₄ particles when decorated with Ag nanowires.

To understand the photocatalytic activity of a photocatalyst, it is necessary to evaluate the recombination behavior of photogenerated electron-hole pairs in the photocatalyst. PL spectroscopy is an important technique that can be used to investigate the electron-hole recombination in the photocatalyst. The PL intensity is in proportion to the recombination rate of photogenerated electrons and holes. Fig. 7 shows the PL spectra of CuBi₂O₄ and Ag-CuBi₂O₄ measured at an excitation wavelength of 320 nm. For bare CuBi₂O₄, several obvious PL emission peaks are observed in the wavelength region of 400–550 nm. In contrast, the intensity of the PL emission peaks from Ag-CuBi₂O₄ is clearly decreased, implying a decrease in the electron-hole recombination. The effective inhibition of electron-hole recombination is ascribed to the electron transfer from CuBi₂O₄ particles to Ag nanowires. As a result, there are more photogenerated electrons and holes in Ag-CuBi₂O₄ composite participating in the photocatalytic reactions.

The separation and transfer behavior of photogenerated electrons and holes was further verified by measuring photocurrent response spectra and EIS spectra of the photocatalysts. Fig. 8(a) shows the
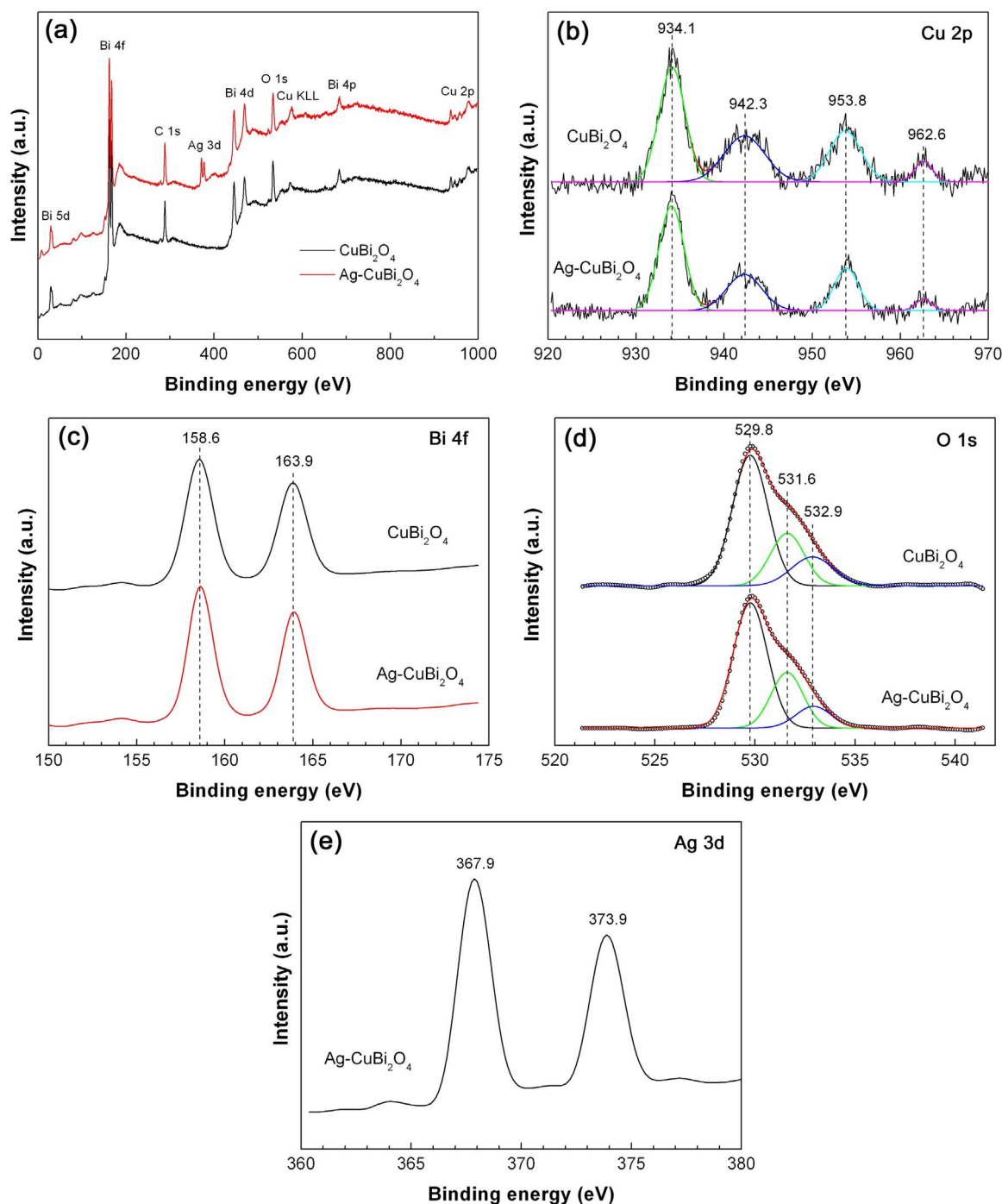
Fig. 5. XPS spectra of $CuBi_2O_4$ and $Ag-CuBi_2O_4$. (a) XPS survey spectra; (b) Cu 2p XPS spectra; (c) Bi 4f XPS spectra; (d) O 1s XPS spectra; (e) Ag 3d XPS spectrum.

transient photocurrent responses of $CuBi_2O_4$ and $Ag-CuBi_2O_4$ recorded for several on-off cycles under intermittent irradiation of simulated sunlight. For both the samples, an obvious photocurrent is observed upon turning the simulated sunlight on. Moreover, the transient photocurrent responses appear to be highly reproducible when the light is repeatedly switched between on and off. Compared to bare $CuBi_2O_4$, $Ag-CuBi_2O_4$ composite displays an enhanced photocurrent density, indicating an increased separation efficiency of photogenerated electron-hole pairs. Fig. 8(b) shows the Nyquist plots of the EIS spectra for $CuBi_2O_4$ and $Ag-CuBi_2O_4$, which exhibit a typical semicircle shape. The semicircle diameter corresponds to the charge-transfer resistance at the electrode/electrolyte interface. It is seen that the Nyquist plot of $Ag-CuBi_2O_4$ has a smaller semicircle diameter than that of bare $CuBi_2O_4$,

implying a smaller charge-transfer resistance for the composite. The smaller charge-transfer resistance suggests more efficient separation of photogenerated chargers and fast interface charge transfer occurring in the composite.

Fig. 9(a) shows the photocatalytic degradation of RhB over $CuBi_2O_4$ and $Ag-CuBi_2O_4$ (0.1 g photocatalyst) as a function of irradiation time t. It is obvious that $Ag-CuBi_2O_4$ exhibits an enhanced photocatalytic activity compared to bare $CuBi_2O_4$. The degradation percentage of RhB is defined as $(C_0 - C_t)/C_0 \times 100\%$, where C_0 and C_t represent the initial RhB concentration and the remaining RhB concentration after irradiation for time t, respectively. After 60 min of photocatalysis, the degradation percentage of the dye reaches 91.7% for $Ag-CuBi_2O_4$, but only 74.2% for bare $CuBi_2O_4$. Fig. 9(b) shows the plots of $Ln(C_t/C_0)$ vs.

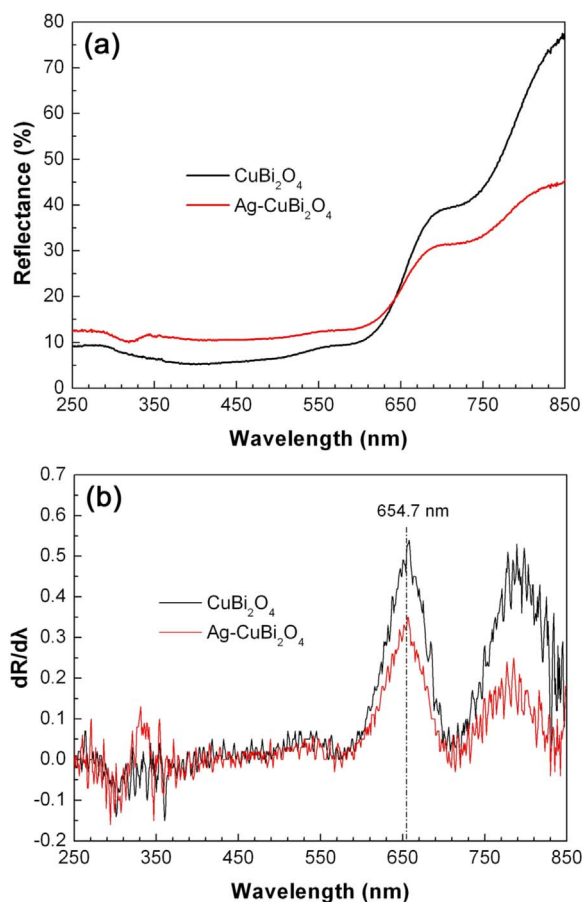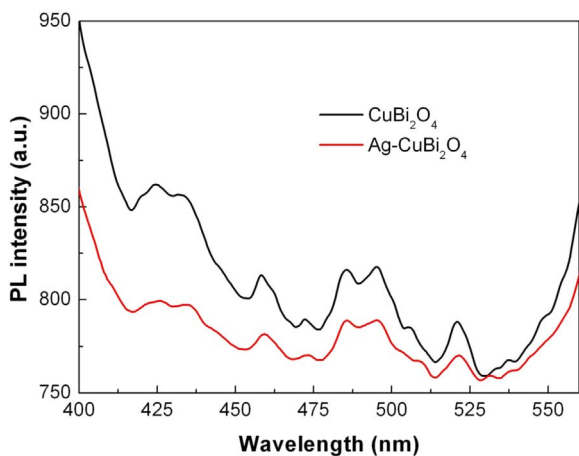**Fig. 6.** (a) UV–vis DRS spectra of $CuBi_2O_4$ and $Ag-CuBi_2O_4$. (b) The corresponding first derivative spectra.

Fig. 8. (a) Transient photocurrent responses of $CuBi_2O_4$ and $Ag-CuBi_2O_4$. (b) Nyquist plots of the EIS spectra for $CuBi_2O_4$ and $Ag-CuBi_2O_4$.

Fig. 7. PL spectra of $CuBi_2O_4$ and $Ag-CuBi_2O_4$.

irradiation time t for $CuBi_2O_4$ and $Ag-CuBi_2O_4$. It is seen that the variation of $Ln(C_t/C_0)$ with t for both the samples follows a linear trend with good correlation coefficients R^2 ($R^2 > 0.99$), suggesting that the time-dependent photocatalytic degradation of RhB follows pseudo-first-order kinetics, i.e., $Ln(C_t/C_0) = -k_{app}t$, where k_{app} is the apparent first-order reaction rate constant (min^{-1}) [41]. The rate constant k_{app} is obtained from the slope of the regression lines as $0.0213\ min^{-1}$ for $CuBi_2O_4$ and $0.04099\ min^{-1}$ for $Ag-CuBi_2O_4$. This implies that $Ag-CuBi_2O_4$ has a photocatalytic activity 1.9 times higher than that of bare $CuBi_2O_4$. The effect of photocatalyst ($Ag-CuBi_2O_4$) dosage on the degradation percentage of RhB after irradiation for 60 min was also

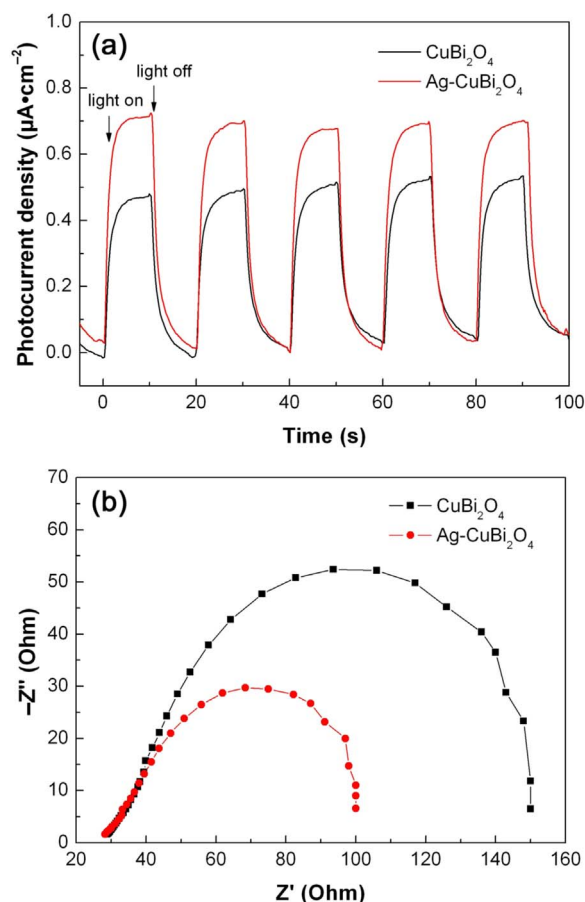investigated, as shown in Fig. 9(c). With increasing the photocatalyst dosage, the dye degradation is seen to increase initially and then exhibits a decreasing trend, where the optimum loading of the photocatalyst is about 0.05–0.1 g in 100 mL RhB solution. In general, an appropriate increase in photocatalyst dosage can offer more active sites for the photocatalytic reaction. However, when the photocatalyst is added in excess, the light transmission is reduced due to the enhanced photon scattering from photocatalyst particles. As a result, the light availability is decreased, thus leading to a decrease in the photocatalytic efficiency at high photocatalyst loading. The degradation of phenol over $CuBi_2O_4$ and $Ag-CuBi_2O_4$ was also investigated, as shown in Fig. 9(d). Both $CuBi_2O_4$ and $Ag-CuBi_2O_4$ also exhibit pronounced photocatalytic activity toward the phenol degradation, and moreover, an enhanced photocatalytic activity is observed for $Ag-CuBi_2O_4$. After 60 min of photocatalysis, the degradation percentage of phenol reaches 79.4% for $Ag-CuBi_2O_4$ composite and 62.8% for bare $CuBi_2O_4$. Compared to RhB, phenol exhibits a relatively smaller degradation efficiency.

The photocatalytic stability of a photocatalyst is an important parameter used for evaluating its practical application. To investigate the photocatalytic stability of $Ag-CuBi_2O_4$, it was repeatedly used for the recycling photocatalytic experiment four times. After the completion of the first cycle of the photocatalysis, the photocatalyst was collected and washed with water, followed by drying in a thermostat drier. The recovered photocatalyst was loaded in the fresh RhB solution for the next cycle of the photocatalytic experiment under the same conditions. The obtained result of the recycling photocatalytic experiment is shown in Fig. 10, revealing an excellent recycling stability of $Ag-CuBi_2O_4$. At the 4th cycle of the photocatalysis, the degradation percentage of RhB still reaches a high value of 89.3% after 60 min of

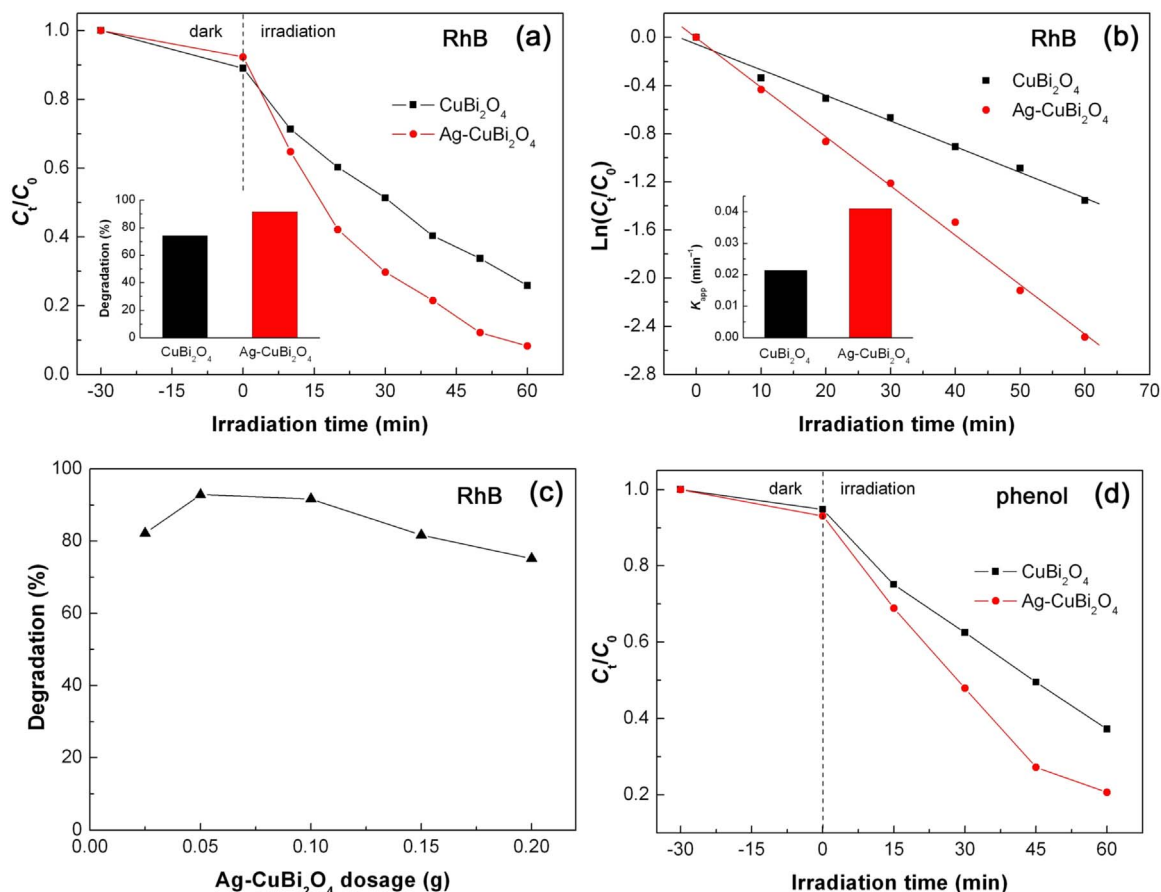**Fig. 9.** (a) Photocatalytic degradation of RhB over $CuBi_2O_4$ and $Ag-CuBi_2O_4$ (0.1 g) as a function of irradiation time *t*. (b) Plots of $Ln(C_t/C_0)$ versus irradiation time *t* for $CuBi_2O_4$ and $Ag-CuBi_2O_4$. (c) Effect of $Ag-CuBi_2O_4$ dosage on the degradation percentage of RhB after irradiation for 60 min. (d) Time-dependent degradation of phenol over $CuBi_2O_4$ and $Ag-CuBi_2O_4$.
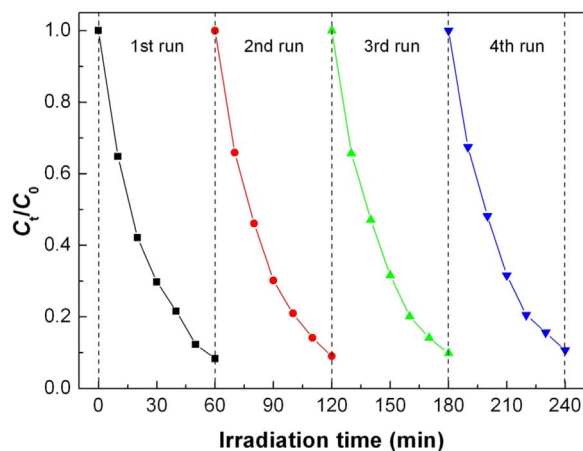

Fig. 10. Photocatalytic degradation of RhB over $Ag-CuBi_2O_4$ for reusing four times.
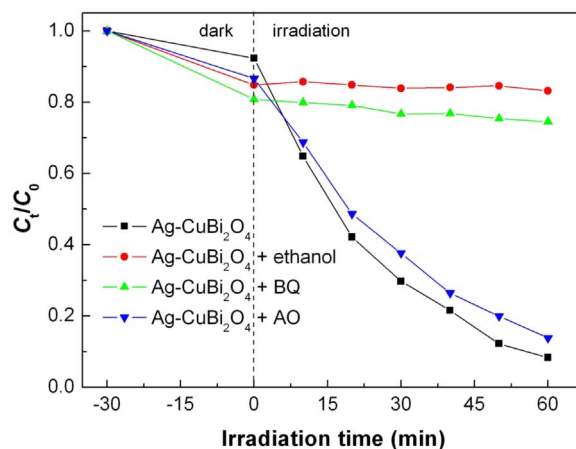

Fig. 11. Effect of ethanol, BQ and AO on the degradation of RhB over $Ag-CuBi_2O_4$.

photocatalysis.

Fig. 11 shows the effect of ethanol, BQ and AO on the degradation of RhB over $Ag-CuBi_2O_4$. It is found that the addition of AO to the reaction solution has only a minor suppression on the degradation of RhB and the dye degradation still maintains a high level of 86.2% after 60 min of photocatalysis, indicating that h^+ is not the dominant reaction species in the photocatalysis. However, when adding ethanol or BQ to the reaction solution, the dye degradation is significantly inhibited. Only 16.8% and 25.5% of the dye are observed to be decolorized on adding ethanol and BQ, respectively, and the decolorization is mainly attributed to the adsorption effect. This implies that the dye degradation is

highly correlated with $\cdot OH$ and $\cdot O_2^-$.

Fig. 12 shows the PL spectra of the TPA solution after reaction for 30 min over $Ag-CuBi_2O_4$ without and with adding ethanol, BQ and AO. The PL spectrum of the blank TPA solution without photocatalyst is also shown in Fig. 12, from which almost no PL signal is observed. On irradiation in the presence of $Ag-CuBi_2O_4$, the TPA solution shows a strong PL signal at around 429 nm, suggesting that $\cdot OH$ is produced over the simulated-sunlight-irradiated $Ag-CuBi_2O_4$. When adding AO to the TPA reaction solution, the PL signal intensity undergoes a slight decrease, implying that AO has only a slight effect on the yield of $\cdot OH$. On the addition of ethanol or BQ, the PL signal disappears almost
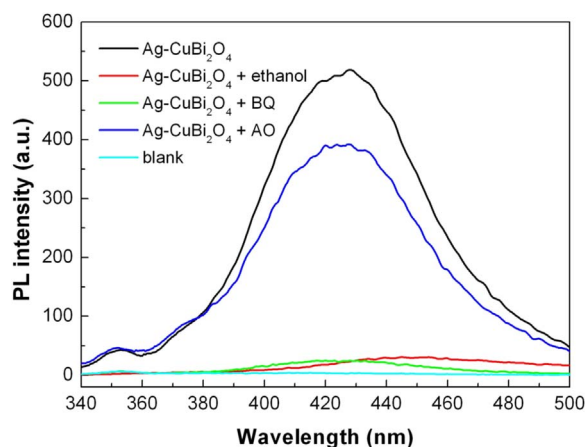
Fig. 12. PL spectra of the TPA solution after reaction for 30 min over Ag-CuBi$_2$O$_4$ without and with adding ethanol, BQ and AO.

Fig. 14. Schematic illustration of the potential energy diagram for Ag-CuBi$_2$O$_4$ composite.

completely, which implies that •OH is quenched by ethanol or BQ. Based on the experimental results of the effect of ethanol, BQ and AO on the yield of •OH and the degradation of RhB, it is concluded that •OH is the dominant reactive species causing the dye degradation.

In order to understand the photocatalytic mechanism of Ag-CuBi$_2$O$_4$ composite, it is necessary to determine the potential energy diagram of the composite. The flat band potential of CuBi$_2$O$_4$ can be determined according to the Mott–Schottky equation [42].

$$\frac{1}{C^2} = \left(\frac{2}{e \varepsilon_r \varepsilon_0 N_d A} \right) \left(V - V_{FB} - \frac{kT}{e} \right) \tag{1}$$

where C is the space charge capacitance, e is the electron charge, ε_r is the relative permittivity, ε_0 is the vacuum permittivity, N_d is the majority carrier density, A is the electrode surface area, V is the applied potential, V_{FB} is the flat band potential, k is the Boltzmann constant, and T is the absolute temperature. Generally, the temperature-dependent correction term, kT/e, is very small and can be negligible. The space charge capacitance of CuBi$_2$O$_4$ is derived by measuring electrochemical impedance as a function of applied potential in the dark. Fig. 13 shows the Mott–Schottky plots of CuBi$_2$O$_4$ obtained at two frequencies (5000 and 10,000 Hz). The linear portion of the plots is extrapolatted to the potential axis to yield the flat band potential (V_{FB}). It is obvious that a similar V_{FB} value is obtained at different frequencies, which is found to be 0.82 V vs. SCE. The potential is measured against an SCE reference at pH = 7 and converted to the potential at normal hydrogen electrode (NHE) by using V(NHE) = V(SCE) + 0.059 pH + 0.242. Thus the flat band potential of CuBi$_2$O$_4$ is obtained as 1.48 V vs. NHE. The negative slope implies that CuBi$_2$O$_4$ is a p-type
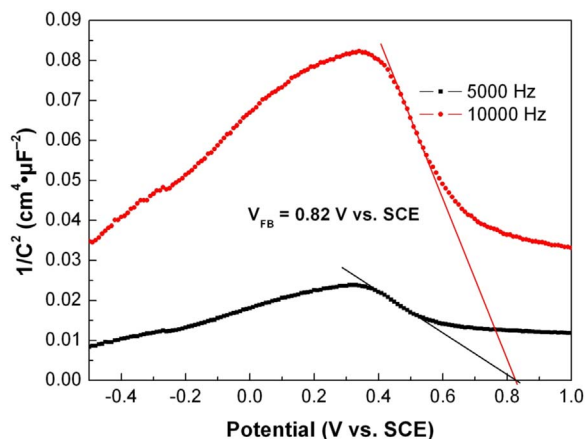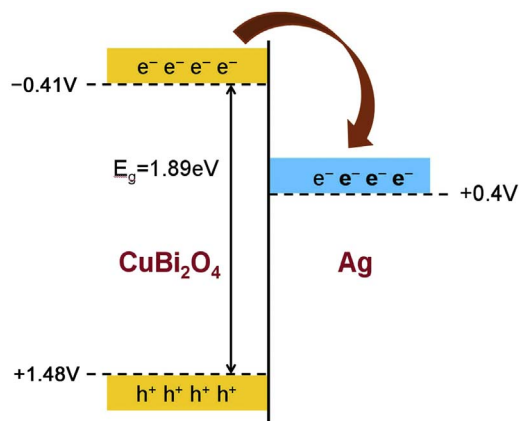

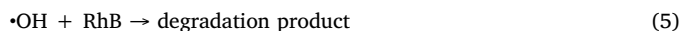**Fig. 13.** Mott–Schottky plots of CuBi$_2$O$_4$ obtained at 5000 and 10,000 Hz.

semiconductor. Assuming the gap between the flat band potential and the top edge of the valence band (VB) is negligible, the VB potential of CuBi$_2$O$_4$ is estimated as 1.48 V vs. NHE. The conduction band (CB) of CuBi$_2$O$_4$ is obtained as −0.41 V vs. NHE by considering its bandgap energy of 1.89 eV.

Fig. 14 schematically shows the potential energy diagram of Ag-CuBi$_2$O$_4$ composite. The Fermi level of Ag is located at +0.4 V vs. NHE [43], which is positive to the CB potential of CuBi$_2$O$_4$. This implies that, from a thermodynamic point of view, the photogenerated electrons tend to migrate from CuBi$_2$O$_4$ particles to Ag nanowires. The electron transfer process results in a decrease in the recombination rate of electron-hole pairs, and thus more charge carriers are able to participate in the photocatalytic reactions. As a result, Ag-CuBi$_2$O$_4$ composite exhibits an enhanced photocatalytic activity compared to bare CuBi$_2$O$_4$. In the Ag-CuBi$_2$O$_4$ photocatalytic system, •OH is confirmed to be the dominant reactive species responsible for the dye degradation. Generally, there are several possible paths to produce •OH in a photocatalytic system. Here the generation of •OH is highly dependent on •O$_2^-$, because when •O$_2^-$ is quenched by BQ, almost no •OH is observed to be formed. The main reactions involved in the photocatalytic process can be briefly described as follows.

$$CuBi_2O_4 + h\nu \rightarrow CuBi_2O_4 \ (e^- + h^+) \tag{2}$$

$$O_2 + e^- \rightarrow \cdot O_2^- \tag{3}$$

$$H_2O_2 + \cdot O_2^- \rightarrow \cdot OH + OH^- + O_2 \tag{4}$$

$$\cdot OH + RhB \rightarrow degradation \ product \tag{5}$$
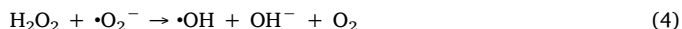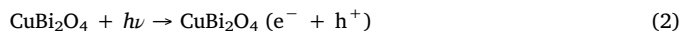
4. Conclusions

Ag nanowires of 30 nm in diameter and 0.8–1.5 μm in length were successfully assembled onto the surface of CuBi$_2$O$_4$ particles (350–700 nm) via a hydrothermal reaction route. In the as-prepared Ag-CuBi$_2$O$_4$ composite, photogenerated electrons tend to migrate from CuBi$_2$O$_4$ particles to Ag nanowires. This electron transfer process leads to a decrease in the recombination of electron-hole pairs, and thus more photogenerated holes and electrons are able to participate in the photocatalytic reactions. As a result, Ag-CuBi$_2$O$_4$ composite is expected to exhibit an enhanced photocatalytic activity. It is shown that the photocatalytic activity of Ag-CuBi$_2$O$_4$ is much higher than that of bare CuBi$_2$O$_4$ toward the degradation of RhB or phenol under simulated-sunlight irradiation. When adding ethanol to the reaction solution, the dye degradation is found to be completely suppressed, and furthermore, the addition of ethanol leads to the quenching of •OH radicals. This suggests that •OH is the dominant reactive species in the present Ag-CuBi$_2$O$_4$ photocatalytic system.

Acknowledgements

References

[1] N. Henry, O. Mentre, J.C. Boivin, F. Abraham, Chem. Mater. 13 (2001) 543–551.
[2] B.D. White, W.M. Patzold, J.J. Neumeier, Phys. Rev. B 82 (2010) 094439.
[3] K. Yoshii, T. Fukuda, H. Akahama, J. Kano, T. Kambe, N. Ikeda, Physica C 471 (2011) 766–769.
[4] V.M. Denisov, L.A. Irtyugo, L.T. Denisova, S.D. Kirik, L.G. Chumilina, Phys. Solid State 54 (2012) 1943–1945.
[5] A.A. Ensafi, N. Ahmadi, B. Rezaei, J. Alloy. Compd. 652 (2015) 39–47.
[6] Y.C. Zhang, H. Yang, W.P. Wang, H.M. Zhang, R.S. Li, X.X. Wang, R.C. Yu, J. Alloy. Compd. 684 (2016) 707–713.
[7] L. Zhu, P. Basnet, S.R. Larson, L.P. Jones, J.Y. Howe, R.A. Tripp, Y. Zhao, ChemistrySelect 1 (2016) 1518–1524.
[8] D. Kang, J.C. Hill, Y. Park, K.S. Choi, Chem. Mater. 28 (2016) 4331–4340.
[9] M. Wang, J. Zai, X. Wei, W. Chen, N. Liang, M. Xu, R. Qi, X. Qian, CrystEngComm 17 (2015) 4019–4025.
[10] N.T. Hahn, V.C. Holmberg, B.A. Korgel, C.B. Mullins, J. Phys. Chem. C 116 (2012) 6459–6466.
[11] S.P. Berglund, F.F. Abdi, P. Bogdanoff, A. Chernseddine, D. Friedrich, R. van de Krol, Chem. Mater. 28 (2016) 4231–4242.
[12] Y. Nakabayashi, M. Nishikawa, Y. Nosaka, Electrochim. Acta 125 (2014) 191–198.
[13] R. Patil, S. Kelkar, R. Naphade, S. Ogale, J. Mater. Chem. A 2 (2014) 3661–3668.
[14] D.W. Cao, N. Nasori, Z.J. Wang, Y. Mi, L.Y. Wen, Y. Yang, S.C. Qu, Z.G. Wang, Y. Lei, J. Mater. Chem. A 4 (2016) 8995–9001.
[15] Y.H. Choi, K.D. Yang, D.H. Kim, K.T. Nam, S.H. Hong, Mater. Lett. 188 (2017) 192–196.
[16] S. Anandan, G.J. Lee, C.K. Yang, M. Ashokkumar, J.J. Wu, Chem. Eng. J. 183 (2012) 46–52.
[17] W.D. Oha, S.K. Lua, Z. Dong, T.T. Lim, Nanoscale 7 (2015) 8149–8158.
[18] G. Sharma, Z. Zhao, P. Sarker, B.A. Nail, J. Wang, M.N. Huda, F.E. Osterloh, J. Mater. Chem. A 4 (2016) 2936–2942.
[19] Y. Zhang, Y. Xie, J. Li, G. Yang, T. Bai, J. Wang, J. Alloy. Compd. 580 (2013) 172–175.
[20] Y. Xie, Y. Zhang, G. Yang, C. Liu, J. Wang, Mater. Lett. 107 (2013) 291–294.
[21] J.W. Zhang, Y.Y. Jiang, J. Mater. Sci. -Mater. Electron. 26 (2015) 4308–4312.
[22] S. Anandan, N. Pugazhenthiran, G.J. Lee, J.J. Wu, J. Mol. Catal. A 379 (2013) 112–116.
[23] X.J. Chen, Y.Z. Dai, J. Guo, Mater. Lett. 161 (2014) 251–254.
[24] Y.F. Zhang, G.F. Li, H.P. Zhao, F. Tian, S.Q. Xiao, R. Chen, CrystEngComm 15 (2013) 8159–8165.
[25] H.W. Huang, K. Xiao, Y. He, T.R. Zhang, F. Dong, X. Du, Y.H. Zhang, Appl. Catal. B 199 (2016) 75–86.
[26] H.W. Huang, X.W. Li, J.J. Wang, F. Dong, P.K. Chu, T.R. Zhang, Y.H. Zhang, ACS Catal. 5 (2015) 4094–4103.
[27] H.W. Huang, X. Han, X.W. Li, S.C. Wang, P.K. Chu, Y.H. Zhang, ACS Appl. Mater. Interfaces 7 (2015) 482–492.
[28] Y. Zhang, Y. Xie, J. Li, T. Bai, J. Wang, J. Sol-Gel Sci. Technol. 71 (2014) 38–42.
[29] W. Liu, S. Chen, S. Zhang, W. Zhao, H. Zhang, X. Yu, J. Nanopart. Res. 12 (2010) 1355–1366.
[30] M. Nishikawa, S. Hiura, Y. Mitani, Y. Nosaka, J. Photochem. Photobiol. A 262 (2013) 52–56.
[31] E. Abdelkader, L. Nadjia, B. Ahmed, Appl. Surf. Sci. 258 (2012) 5010–5024.
[32] A. Elaziouti, N. Laouedj, A. Bekka, R.N. Vannier, Sci. Technol. 39 (2014) 9–22.
[33] Y. Deng, Y. Chen, B. Chen, J. Ma, Preparation, characterization and photocatalytic activity of CuBi$_2$O$_4$/NaTaO$_3$ coupled photocatalysts, J. Alloy. Compd. 559 (2013) 116–122.
[34] W. Liu, S. Chen, H. Zhang, X. Yu, J. Exp. Nanosci. 6 (2011) 102–120.
[35] Y.C. Ye, H. Yang, R.S. Li, X.X. Wang, J. Sol-Gel Sci. Technol. 82 (2017) 509–518.
[36] T. Okuno, G. Kawamura, H. Muto, A. Matsuda, J. Solid State Chem. 235 (2016) 132–138.
[37] V. Vaiano, G. Iervolino, D. Sannino, J.J. Murcia, M.C. Hidalgo, P. Ciambelli, J.A. Navio, Appl. Catal. B 188 (2016) 134–146.
[38] F. Wang, H. Yang, Y.C. Zhang, R.S. Li, Int. J. Mater. Res. 108 (2017) 298–307.
[39] M. Zhou, H. Yang, T. Xian, R.S. Li, H.M. Zhang, X.X. Wang, J. Hazard. Mater. 289 (2015) 149–157.
[40] W.P. Wang, H. Yang, T. Xian, J.L. Jiang, Mater. Trans. 53 (2012) 1586–1589.
[41] I.K. Konstantinou, T.A. Albanis, Appl. Catal. B 49 (2004) 1–14.
[42] F. Cardon, W.P. Gomes, J. Phys. D: Appl. Phys. 11 (1978) L63–L67.
[43] P.V. Kamat, J. Phys. Chem. C 111 (2007) 2834–2860.